First-principles study of Zintl aluminide SrAl_{2}

Alexander Slepko and Alexander A. Demkov

Phys. Rev. B **85**, 195462 — Published 29 May 2012

DOI: 10.1103/PhysRevB.85.195462

First principles study of Zintl aluminide $SrAl_2$

Alexander Slepko and Alexander A. Demkov[1]
Department of Physics, The University of Texas at Austin, Austin, Texas 78712, USA

Zintl intermetallics hold promise for applications in oxide/semiconductor epitaxy. We report a density functional investigation of the Zintl phase strontium aluminide $SrAl_2$. We calculate electronic properties of the orthorhombic and cubic phases. For the orthorhombic phase we calculate the work function and surface energy for (001), (010) and (100) orientated surfaces. The work function varies between 2.0 eV and 4.1 eV, and is determined by the predominant atomic species on the surface. The surface energy ranges from 320 erg/cm^2 to 1842 erg/cm^2. We also calculate the elastic constants.

I. INTRODUCTION

Silicon based complementary metal oxide semiconductor (CMOS) technology is rapidly approaching its physical limits [1, 2]. The most recent problem has been the thickness of the SiO_2 gate oxide that couldn't be reduced below the critical thickness of four atomic layers without losing its insulating properties. The current solution to the problem is to use a gate oxide with a dielectric constant higher than that of SiO_2 such as hafnia, allowing for higher gate capacitance albeit operating well above the physical size limit [3]. Using crystalline perovskites as a gate dielectric may offer further gate stack scaling [4]. For comparison, the relative dielectric constant of SiO_2 is approximately 4, while that of $SrTiO_3$ is 2000 [5]. However, despite the promise, incorporating crystalline oxides on silicon imposes several difficulties [6, 7]. One arises from the abrupt change in the nature of chemical bonding across the Si/dielectric interface. While Si forms a covalent bond network, bonding in a perovskite such as *i.e.*, $SrTiO_3$ is largely ionic. Thus, an epitaxial oxide/semiconductor interface is likely to suffer from high interfacial energy caused by the transition from the ionic to covalent bond type. This in turn prevents the oxide from wetting the Si substrate necessary for a layer by layer growth of high quality films. In the case of $SrTiO_3$ (STO) on Si, the surface energy of STO plus the energy of the interface should not exceed the surface energy of Si of ~1700 erg/cm^2 to achieve wetting. With the STO surface energy ranging from 800 to 2000 erg/cm^2 depending on the environment, one needs an interface with the energy below 900 erg/cm^2 to wet silicon [7]. One possible solution to this problem is incorporating a mediating interfacial layer that can accommodate both the oxide's ionic and semiconductor's covalent bonding. For STO on Si this has been realized with the $SrSi_2$ template that has the stoichiometry of a bulk Zintl-Klemm intermetallic compound [8, 9]. These unusual materials have been first characterized by Eduard Zintl in the 1930s [10]. Typically, Zintl phases are of the form $A_aX_x = (A^{n+})_a[X^{(an/x)-}]_x$, where the atomic species A, called the

[1] demkov@physics.utexas.edu

'active' metal, is of the first or second main group in the periodic table and species X is an electronegative metal or a semimetal of the third or fourth main group. The active metal donates its valence electrons to the electronegative metal, and both species can build seemingly independent sublattices in the so-called Zintl-phase. The sublattice of species X typically assumes the coordinated structure capable of accommodating extra electrons in its bonds (Zintl-Klemm rules [11]), and thus effectively shows the covalent bonding character of the isovalent element. For example, in the prototypical Zintl phase NaTl, the Tl sublattice assumes the diamond structure of the neighboring elements Si or C upon receiving the extra electron from Na [11]. Overall, however, the Zintl phase also shows ionic character due to charge transfer. This mixed nature of bonding sometimes called Zintl bonding, allows for mediation between ionically and covalently bonded materials.

Despite their curious nature and possible applications in crystalline oxide epitaxy on semiconductors, a relatively modest body of theoretical work exists on Zintl phases [summarized in Refs. 11-12]. Here we consider theoretically a Zintl phase $SrAl_2$ that may find applications in epitaxy of III-V semiconductors with perovskites [13-14]. It crystallizes in the orthorhombic *Imma* structure under ambient conditions and assumes a cubic *Fd-3m* structure under high pressure [15-16]. Here we focus on the orthorhombic phase. Though hydrogenated $SrAl_2H_2$, where the hydrogen atoms are inserted interstitially, have been recently studied [11, 17], rather little is known about pure $SrAl_2$ besides the crystallographic data. Therefore, a basic study of its physical properties is of practical interest. We report on the electronic, structural and elastic properties of bulk $SrAl_2$ and its low index surfaces. We calculate the work function and surface energy of the (001), (010) and the (100) oriented surfaces of different stoichiometry. For the orthorhombic ground state we also evaluate the elastic tensor.

II. COMPUTATIONAL DETAILS

All calculations are done within the framework of the density functional theory (DFT). We employ the generalized gradient approximation (GGA) with the Perdew-Burke-Ernzerhof functional [18]. To solve the Kohn-Sham equation we use a plane wave expansion of the wave function along with PAW pseudopotentials as implemented in the VASP code [19]. The valence configuration of Sr is $4s^2$, $4p^6$, $5s^2$, and for Al we use $3s^2$, $3p^1$. The Brillouin Zone integration is done using Monkhorst-Pack *k*-point meshes [20]. For primitive cells of orthorhombic and cubic $SrAl_2$ we employ 8×14×8 and 6×6×6 k-point meshes, respectively. Work functions and surface energies are calculated using slab geometry. In these calculations we use 8×14×2, 8×8×2 and 14×8×2 k-point meshes for the (001), (010) and (100) surface models, respectively. The $SrAl_2$ bulk is fully relaxed by optimizing the cell shape, volume and ionic positions. In the slab calculations we only allow for ionic relaxation. We use the kinetic energy cutoff of 500 eV. Together with the chosen k-point meshes energy convergence is 0.01 meV/cell for bulk calculations. Forces are converged to ~10 meV/Å (less than 1 meV/Å in bulk calculations).

III. BULK PORPERTIES

The primitive cells of orthorhombic and cubic $SrAl_2$ are shown in Figure 1. The orthorhombic cell consists of four molecular $SrAl_2$ units, and the cubic cell consists of eight units. The atomic positions in Wyckoff notations are given in Table 1. The theoretical lattice constants of the orthorhombic cell are a=7.916 Å, b= 4.813 Å and c=7.929 Å, which is very close to the experimental values of 7.905 Å, 4.801 Å and 7.974 Å for a,b and c respectively [16]. The Al atoms are 4-fold coordinated by other Al atoms with the bond length varying between 2.78 Å and 2.88 Å. Although the Al sublattice does not form a diamond structure the coordination is consistent with the Zintl-Klemm rules. The theoretical lattice constant of the cubic cell is 8.325 Å (experimental value is 8.291 Å [16]). The cell consists of a diamond Sr sublattice and Al sublattice is formed by corner sharing tetrahedra. In the cubic unit cell Al atoms are six-fold coordinated by other Al atoms with the Al-Al bond length being 2.93 Å.

The electronic density of states (DOS) normalized per $SrAl_2$ molecular unit for both phases is shown in Figure 2, the Fermi level is set at zero energy. The semi-core Sr 4s and 4p states appear at -35 eV and -18 eV, respectively (not in the figure). The Al 3s states appear between -5 eV and -8 eV in both phases. Close to the Fermi level the main contributors to the DOS are Al 3p states, Sr 5s states and l=2 projected (4d) Sr states. The carrier density within $\pm k_B T$ around the Fermi level is 4.9×10^{20} cm^{-3} in the orthorhombic structure, and it is almost three times higher (12.8×10^{20} cm^{-3}) in the cubic structure. To put these numbers in perspective, the carrier concentration in commonly used silicide PtSi is 7.9×10^{20} cm^{-3} [21].

We find that the orthorhombic phase is slightly lower (20 meV per unit $SrAl_2$) in energy than the cubic one. The experimental work by Cordier *et al.* [16] suggests a pressure induced phase transition from the orthorhombic to cubic phase at 60 kbar. Theoretically, the transition pressure then can be deduced from

$$E_c + pV_c - TS_c = E_o + pV_o - TS_o . \qquad (1)$$

The left hand side is the Gibb's free energy of the cubic phase and the right hand side is that of the orthorhombic phase. Ignoring the entropy contribution for the low temperature limit, the left and right hand sides in (1) are equal at the transition pressure p_{trans} which is the slope of the common tangent of the left and right hand side energy in the E-V diagram. We deduce the volume dependence of the energy in the cubic and monoclinic phase using constant volume calculations. For a chosen fixed volume value we fully relax the lattice constants, cell shape and atomic positions. In Fig. 3 we show the binding energy of the cubic and orthorhombic phases as function of volume per $SrAl_2$ unit. The slope of the common tangent is 7.4 kbar, somewhat lower than the previously reported theoretical transition pressure of 18 kbar [22]. In 21 a lower energy cut-off as used and it is not clear what k-point density was used for the Briollouin zone integration. In our convergence tests we find a rather strong dependence of the calculated binding energy on both parameters. We attribute the discrepancy to the differences in the

computational setup. Experimentally, it is also not entirely clear what the transition pressure is. Cordier *et al.* performed their experiments at 60 kbar where the cubic phase was observed. However, the actual phase transition possibly occurs below that pressure. The sample used in this study was most likely polycrystalline, and the temperature is unknown, making a direct comparison difficult. In what follows we focus only on the orthorhombic structure as under ambient conditions it is the lowest energy phase.

IV. SURFACE PROPERTIES

We calculate the surface energy of the low index (001), (010) and (100) $SrAl_2$ surfaces using slab geometry. We use 1×1 surface cell, and $SrAl_2$ slabs are ~15-20 Å thick. Two neighboring slabs are separated by 15 Å vacuum to suppress slab-slab interactions due to the periodic boundary conditions. Our surface models are shown in Fig. 5a-c. We constructed ten different models (enumerated from one to ten in the figure) according to the following procedure. The dashed lines in Fig. 5 indicate how we cleave each of our ten surfaces. For example, in the (001) orientation we cut four surfaces, the first one is terminated with Al atoms at the first dashed line, the second surface is terminated with Sr at the second dashed line and so on. In the (010) orientation we consider two surfaces, model five as shown in Fig. 5 b) and model six with two top Sr atoms removed. In the (100) orientation we consider four surfaces. Models seven, eight and nine are cleaved as indicated in figure 5 c). Model ten is cleaved as model nine; however, two top Sr atoms are removed. Since most of the surface models are not flat on atomic scale, assigning the surface stoichiometry is somewhat arbitrary. However, when counting all atoms in the slab our models one, three, five, eight and ten have same stoichiometry as $SrAl_2$ bulk. However, in models one and eight Al atoms and in models three and ten Sr atoms are facing vacuum. Only model five has a perfectly stoichiometric surface. Our remaining surfaces are Sr-rich (models two and nine) and Al-rich (models four, six and seven).

To estimate the surface energy we use the Gibbs free energy approach [23]:

$$\sigma = \left[E_{slab} - N_{Al}\left(E_{Al} + \mu_{Al}\right) - N_{Sr}\left(E_{Sr} + \mu_{Sr}\right)\right] / 2A\,, \tag{2}$$

where E_{slab} is the energy of the slab, N_X is the number of atomic species X (Al, Sr), and μ_x and E_x are its chemical potential and bulk energy, respectively. The chemical potentials are referenced to bulk energies of metallic Sr and Al. Assuming the equilibrium of the surface with the bulk:

$$\begin{aligned} &\mu_{Sr} + 2\mu_{Al} = H_f = -0.788\,eV \\ &H_f < \mu_{Sr} < 0 \\ &H_f < 2\mu_{Al} < 0 \end{aligned}\,, \tag{3}$$

we can rewrite (2) as a function of the chemical potential μ_{Sr} solely:

$$\sigma = [E_{slab} - N_{Sr}E_{Sr} - N_{Al}(E_{Al} + 0.5H_f) - \mu_{Sr}(N_{Sr} - 0.5N_{Al})]/2A \ , \quad H_f < \mu_{Sr} < 0 \qquad (4)$$

The boundary conditions for μ_{Sr} correspond to Sr-poor experimental conditions for $\mu_{Sr} = H_f$, and Sr-rich conditions for $\mu_{Sr} = 0$. We show the surface energy in Fig. 4 a). Our surface models are indicated in the plot. The surface energy ranges between 320 erg/cm^2 and 1842 erg/cm^2 depending on the chemical environment. Over the entire range of the chemical potential the (100) oriented Sr-rich surface model nine has the lowest energy, it is closely followed by the (001) oriented surface model two of the same stoichiometry. Al-terminated surfaces (models four, six and seven) have approximately 300 erg/cm^2 higher surface energy under Sr-poor conditions, and approximately 900 erg/cm^2 higher surface energy under Sr-rich conditions. The remaining five surfaces have surface energy ranging between 950 erg/cm^2 and 1100 erg/cm^2. This is important when considering the wetting behavior of thin $SrAl_2$ films on a substrate. A possible substrate is STO. Its lattice mismatch to $SrAl_2$ is less than 0.5% for some configurations. The surface energy of STO ranges from 801 erg/cm^2 to 1923 erg/cm^2 depending on the chemical environment [24]. Thus $SrAl_2$ could wet STO for two Sr-rich models with the lowest surface energy. A more detailed study including the interface is necessary to address this question, however, and is under way.

For all $SrAl_2$ surfaces considered above we calculate the work function. The thickness of our $SrAl_2$ slabs is approximately 20 Å which is sufficient to mimic the bulk electronic properties deep inside the slab. We calculate the electrostatic potential in the simulation cell and average it over the x-y plane for each z value, where z runs in the direction normal to the surface. We then averaged the microscopic *V(z)* along the z-axis over the bulk and vacuum regions. The energy difference between the value of thus averaged potential in the vacuum region and the Fermi level of the slab is taken to be the work function. The calculated values of the work function are shown in Fig. 4 b). The labels indicate the model number. We included the work functions of Sr and Al metals for comparison. The x-axis indicates by how many strontium atoms a given slab deviates from the bulk 1:2 stoichiometry. Negative values indicate Al-rich slabs and positive values correspond to Sr-rich slabs. The work function for Al-rich slabs is close to 4.08 eV of Al metal, whereas for Sr-rich models it ranges from 2.6 eV (work function of pure Sr metal) to 2.0 eV. The lowest surface energy models have work functions 2.0 eV [model two in Fig. 4 b, (001) orientation] and 2.6 eV [model nine in Fig. 4 b, (100) orientation]. For the stoichiometric conditions, *i.e.* twice as many Al atoms as Sr atoms in the slab, the work function ranges from 2.2 eV (model ten) to 4.0 eV (model eight). Surface models one and eight have Al atoms closest to vacuum resulting in the highest work function among the stoichiometric models. Models three and ten have Sr atoms closest to vacuum giving the lowest work function among the stoichiometric models. Interestingly, our model five has Sr and Al atoms equally close to the vacuum region. This model has the work function of 3.25 eV, roughly the average of work functions of Sr and Al. The main conclusion we draw from Fig. 4 b) is that the work function

depends mainly on the surface chemistry. For the models with Al at the surface, the work function tends to be close to that of aluminum metal, whereas the work function of surfaces with mainly Sr on top is close to the work function of Sr metal.

V. ELASTIC PROEPRTIES

Because strain plays an important role in epitaxy, we calculate the elastic constants of orthorhombic $SrAl_2$ from first-principles. Generally, the energy of a strained system can be written as a second order expansion in the distortion parameters $\alpha_{i,j}$ [25]:

$$E(V,\alpha) = E(V_0,0) + \frac{V_0}{2}\sum_{a,b,c,d} C_{abcd}\alpha_{ab}\alpha_{cd} \ . \tag{5}$$

The first order term drops out as the expansion is about the ground state (V_0 is the ground state volume of the cell). The second order term is described by the adiabatic elastic constants C_{abcd}. However, the C_{abcd} and α_{ab} are not all independent, and using the Voigt notation, equation (5) can be simplified. There are nine independent elastic constants in an orthorhombic crystal: C_{11}, C_{12}, C_{13}, C_{22}, C_{23}, C_{33}, C_{44}, C_{55}, C_{66}. In order to determine these constants nine independent distortions must be applied to the system. We use the distortions suggested in ref. 25. Equation (5) is valid for small distortions, and to have a measure of "small" we compare the volume changes after applying a specific distortion. Our distortion parameters are within the range ±0.02 with the maximum volume change ±6 $Å^3$ or 2% of V_0. We relax the atomic positions for all distortions. Using a quadratic fit to the calculated binding energy we extract the elastic constants C_{ij}. The results are summarized in table 2. The elastic constants meet the Cauchy mechanical stability requirements [26]. The bulk modulus is given by

$$B = \tfrac{1}{9}\left(C_{11} + C_{22} + C_{33} + 2C_{12} + 2C_{13} + 2C_{23}\right) = 8.12\times10^{11}\, dyn/cm^2 . \tag{6}$$

Interestingly, the bulk modulus of $SrAl_2$ is comparable to aluminum's 7.6×10^{11} dyn/cm^2. The bulk modulus of Sr is only 1.2×10^{11} dyn/cm^2. Unfortunately, no data on the elastic properties of $SrAl_2$ is available in the literature making a comparison impossible.

VI. CONCLUSIONS

In summary, using density functional theory we have theoretically investigated the electronic structure, elastic and surface properties of cubic and orthorhombic $SrAl_2$ using density functional theory. We predict a significant increase in the electric conductivity of the cubic phase compared to the ground state orthorhombic phase. We estimate the transition pressure of the orthorhombic to cubic transformation to be significantly lower than that reported in a recent experimental study. The elastic constants of orthorhombic $SrAl_2$ are reported; the bulk modulus of 8.12×10^{11} dyn/cm^2 makes $SrAl_2$ slightly stiffer than Al metal. The work function and surface energy depend strongly on the surface termination. The Sr terminated surface has lower surface energy and work function close to 2.59 eV of strontium metal, while the Al terminated surface has higher surface energy and work function close to 4.08 eV of Al metal. The work function result

is consistent with the transistor data reported in Ref. 27, where the Al surface of a SrAl Zintl interlayer was used to achieve wetting of $SrTiO_3$ by GaAs.

ACKNOWLEDGEMENTS

This work is supported by the National Science Foundation under Grant DMR1006725, and Texas Advanced Computing Center.

References

1. D. A. Muller, Nature **399**, 758 (1999).

2. T.N. Theis, and P.M. Solomon, *Science* **327**, 1600 (2010).

3. A. A. Demkov and A. Navrotsky Eds., *Materials Fundamentals of Gate Dielectrics*, Springer, 2005.

4. R. Droopad, K. Eisenbeiser, and A. A. Demkov, "High-K Crystalline Gate Dielectrics – An IC Manufacturer's Perspective" in "*Alternative Gate Dielectrics*", H. Huff and D. Gilmer Eds. (Springer, 2004).

5. J. Robertson, Eur. Phys. J. Appl. Phys. **28**, 265 (2004).

6. R. A. McKee, F. J. Walker, M. F. Chisholm, Phys. Rev. Lett. **81**, 3014 (1998).

7. X. Zhang, A.A. Demkov, H. Li, X. Hu, Y. Wei, and J. Kulik, Phys. Rev. B **68**, 125323 (2003).

8. R. A. McKee, F. J. Walker, and M. F. Chisholm, Phys. Rev. Lett. **81**, 3014 (1998).

9. A.A. Demkov and X. Zhang, J. of Appl. Phys. **103**, 103710 (2008).

10. E. Zintl and W. Dullenkopf, Z. Phys. Chem. **B16,** 195 (1932).

11. Thomas Fässler, *Zintl Phases: Principles and Recent Developments*, Vol. 139 (2011).

12. S. M. Kauzlarich, *Chemistry, structure, and bonding of Zintl phases and ions*, VCH Publishers, Inc., 1996.

13. Y. Liang and A. A. Demkov, "Epitaxial Oxide/.Semiconductor Systems" in "*Materials Fundamentals of Gate Dielectrics*", A. A. Demkov and A. Navrotsky Eds. (Springer, 2005).

14. A.A. Demkov, H. Seo, X. Zhang and J. Ramdani, Appl. Phys. Lett. **100**, 071602 (2012).

15. G. Nagorsen, H. Posch, H. Schaefer, A. Weiss, Z. Naturforsch. **24b**, 1191 (1969).

16. G. Cordier, E. Czech, H. Schaefer, Z. Naturforsch. **37b**, 1442 (1982).

17. F. Gingl, T. Vogt, E. Akiba, J. Alloys Compd. **306**, 127 (2000).

18. J. P. Perdew, K. Burke, and M. Ernzerhof, Phys. Rev. Lett. **77**, 3865 (1996).

19. G. Kresse, J. Hafner, Phys. Rev. B **47**, 558 (1993);G. Kresse, J. Furthmüller, Comput. Mat. Sci. **6**, 15 (1996); G. Kresse, J. Furthmüller, Phys. Rev. B **54**, 11169 (1996); G. Kresse, J. Hafner, J. Phys: Condens. Matt. **6**, 8245 (1994); G. Kresse, D. Joubert, Phys. Rev. B **59**, 1758 (1999).

20. H. J. Monkhorst, J. D. Pack, Phys. Rev. B **13**, 5188 (1976).

21. A. Slepko and A.A. Demkov, Phys. Rev. B **85**, 035311 (2012).

22. S. Kal, E. Stoyanov, J.-P. Belieres, T. L. Groy, R. Norrestam, U. Häussermann, J. Sol. St. Chem. **181**, 3016 (2008).

23. G.-X. Qian, R. M. Martin, D. J. Chadi, Phys. Rev. B **38**, 11 (1988).

24. A. A. Demkov, Phys. Status Solidi B 226, 57 (2001).

25. D. C. Wallace, Solid State Physics **25**, 302 (1970).

26.O. Beckstein, J. E. Klepeis, G. L. W. Hart, O. Pankratov, Phys. Rev. B 63, 134112 (2001).

27. K. Eisenbeiser, R. Emrick, R. Droopad, Z. Yu, J. Finder, S. Rockwell, J. Holmes, C. Overgaard, and W. Ooms, IEEE Electron Device Lett. **23**, 300 (2002).

Table 1: Atomic positions in Wyckoff notation in orthorhombic and cubic $SrAl_2$.

Orthorhombic	**Cubic**
4 Sr 4*e*	8 Sr 8*a*
8 Al 8*i*	16 Al 16*d*

Table 2: Elastic constants and bulk modulus of orthorhombic $SrAl_2$. The elastic constants meet the Cauchy mechanical stability requirements [26]. The bulk modulus is close to that of Al metal (7.6 dyn/cm^2).

	elastic constant [10^{11} dyn/cm^2]
C_{11}	8.55
C_{12}	8.76
C_{13}	7.68
C_{22}	9.01
C_{23}	7.91
C_{33}	6.84
C_{44}	4.28
C_{55}	3.51
C_{66}	3.50
B	8.12

Figure Captions:

Fig. 1: Primitive cells of orthorhombic (a) and cubic (b) $SrAl_2$. The experimental lattice constants are 7.916 Å × 4.813 Å × 7.929 Å for the orthorhombic cell, and 8.291 Å for the cubic cell. The smaller balls are aluminum atoms, the larger balls are strontium atoms.

Fig. 2: Electronic density of states of orthorhombic (top) and cubic (bottom) $SrAl_2$. The electron carrier density at the Fermi level is three times lower in orthorhombic $SrAl_2$ compared to the cubic phase.

Fig. 3: Binding energy of the cubic and orthorhombic $SrAl_2$ as a function of volume per chemical $SrAl_2$ unit. The slope of the common tangent is 7.4 kbar which is the theoretical transition pressure from orthorhombic to cubic phase.

Fig. 4:

a) Surface energy of orthorhombic $SrAl_2$ as a function of the chemical potential of Sr. The data labels indicate our model numbers. Sr-terminated surfaces tend to have lower surface energy than the stoichiometric or Al-terminated surfaces. The running numbers indicate the model.

b) Work function of orthorhombic $SrAl_2$. The x-axis shows the deviation of the slab from the $SrAl_2$ stoichiometry. The data labels indicate the model number. The work function is strongly termination dependent.

Fig. 5: Surface models with (001) (a) orientation, (010) (b) orientation and (100) (c) orientation. From the three models shown we deduce ten surface models in total. The dashed lines indicate how we cleave our surfaces. In total we have four (001) oriented surface models, two (010) oriented surface models and four (100) oriented surface models.

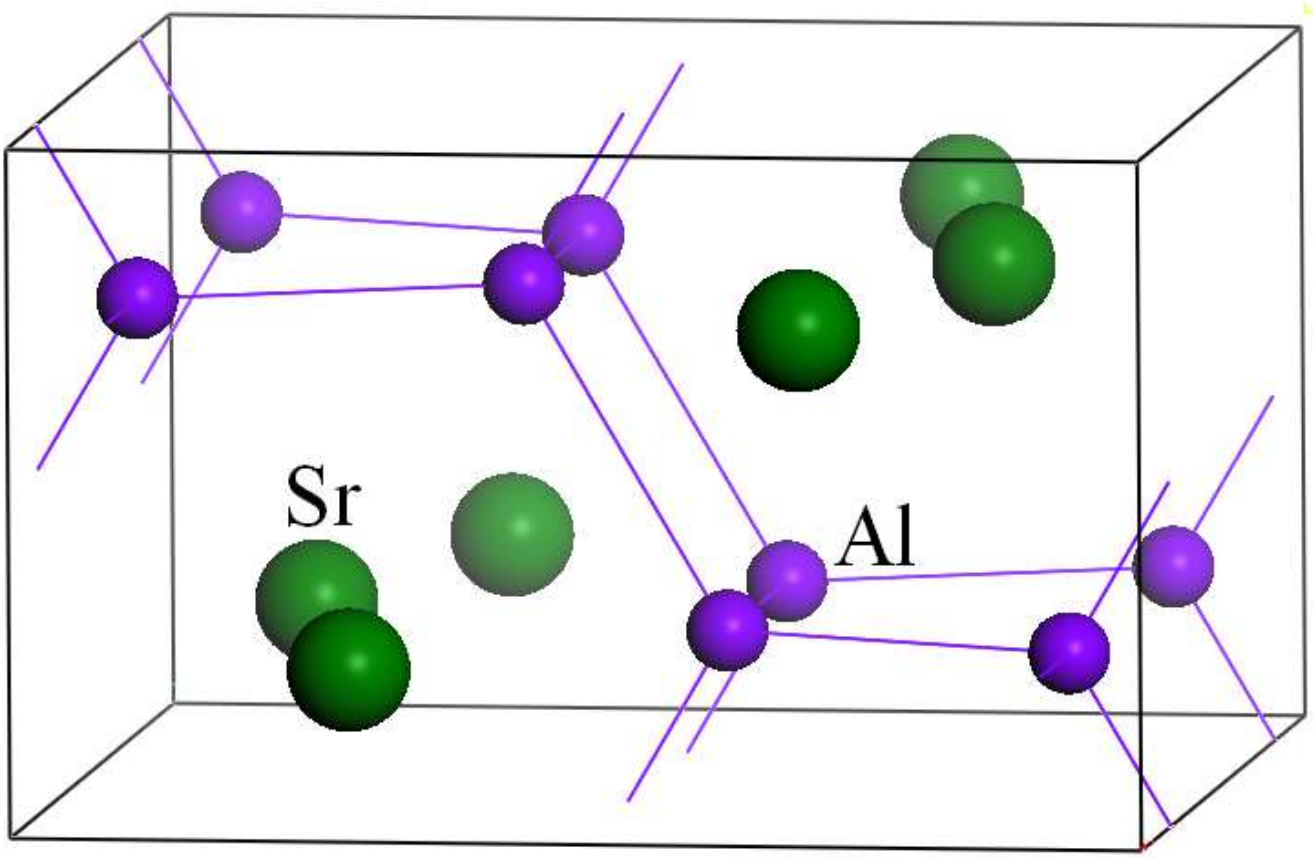

Figure 1a BP11518 11MAY2012

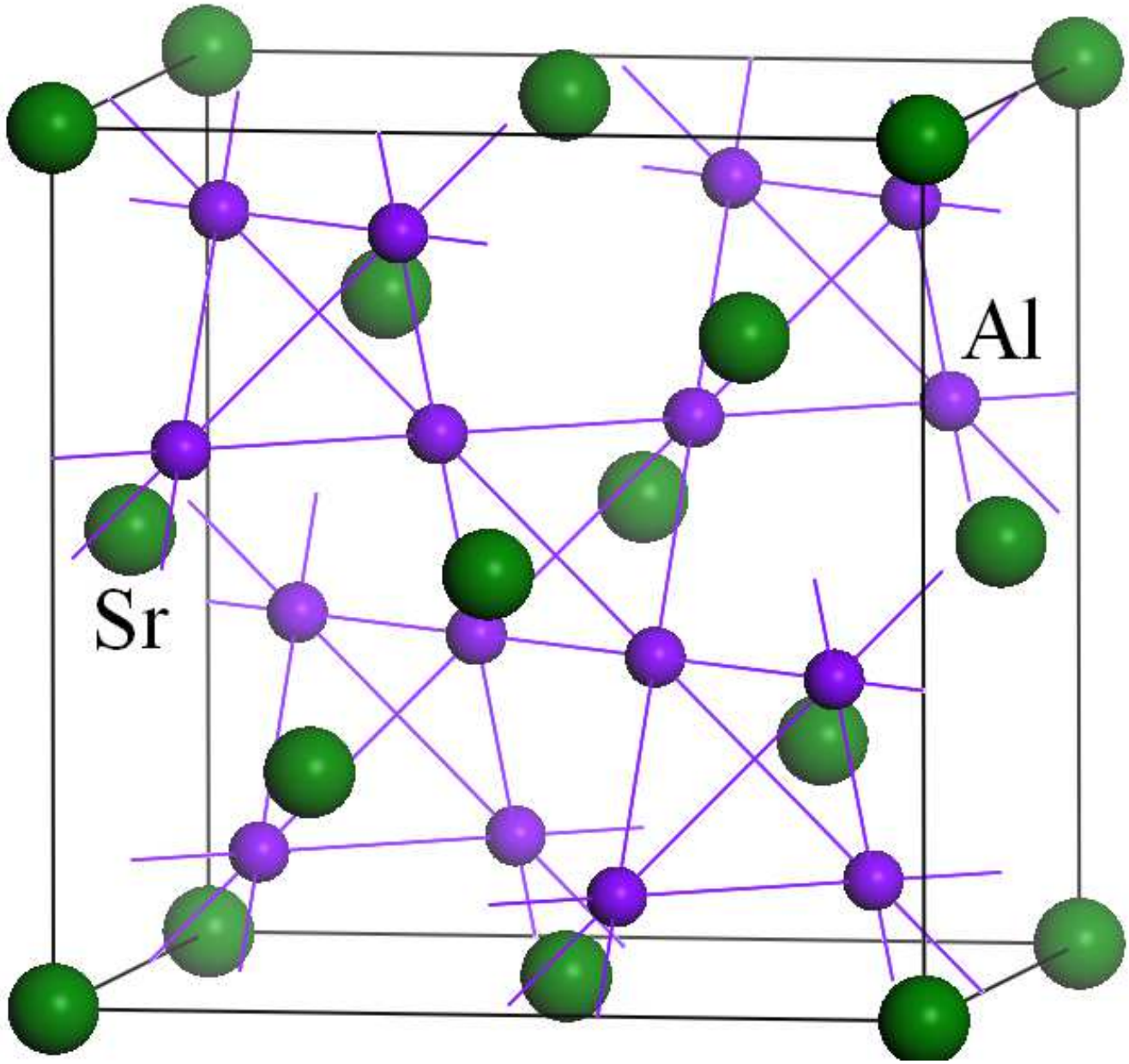

Figure 1b BP11518 11MAY2012

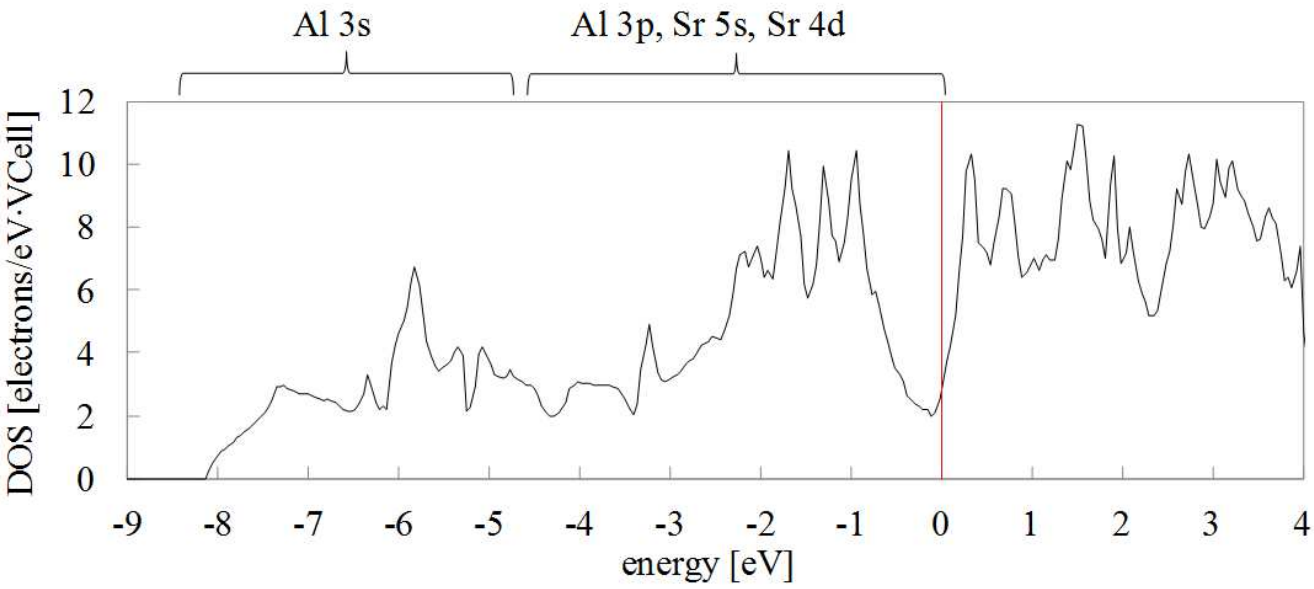

Figure 2a BP11518 11MAY2012

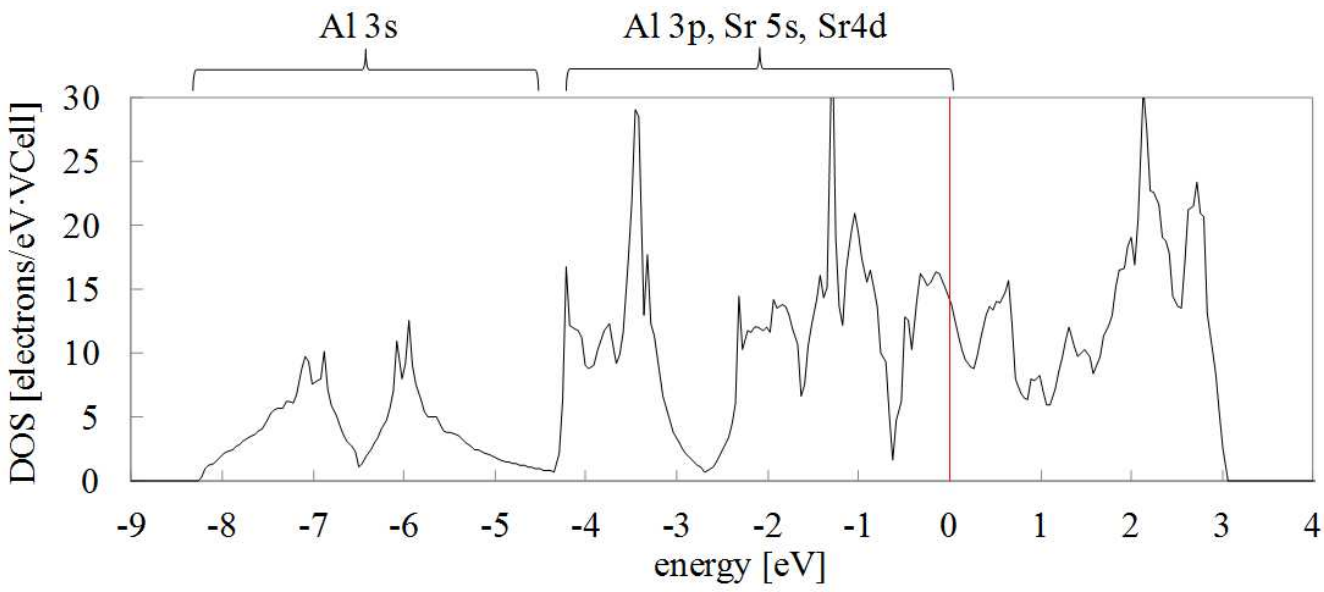

Figure 2b BP11518 11MAY2012

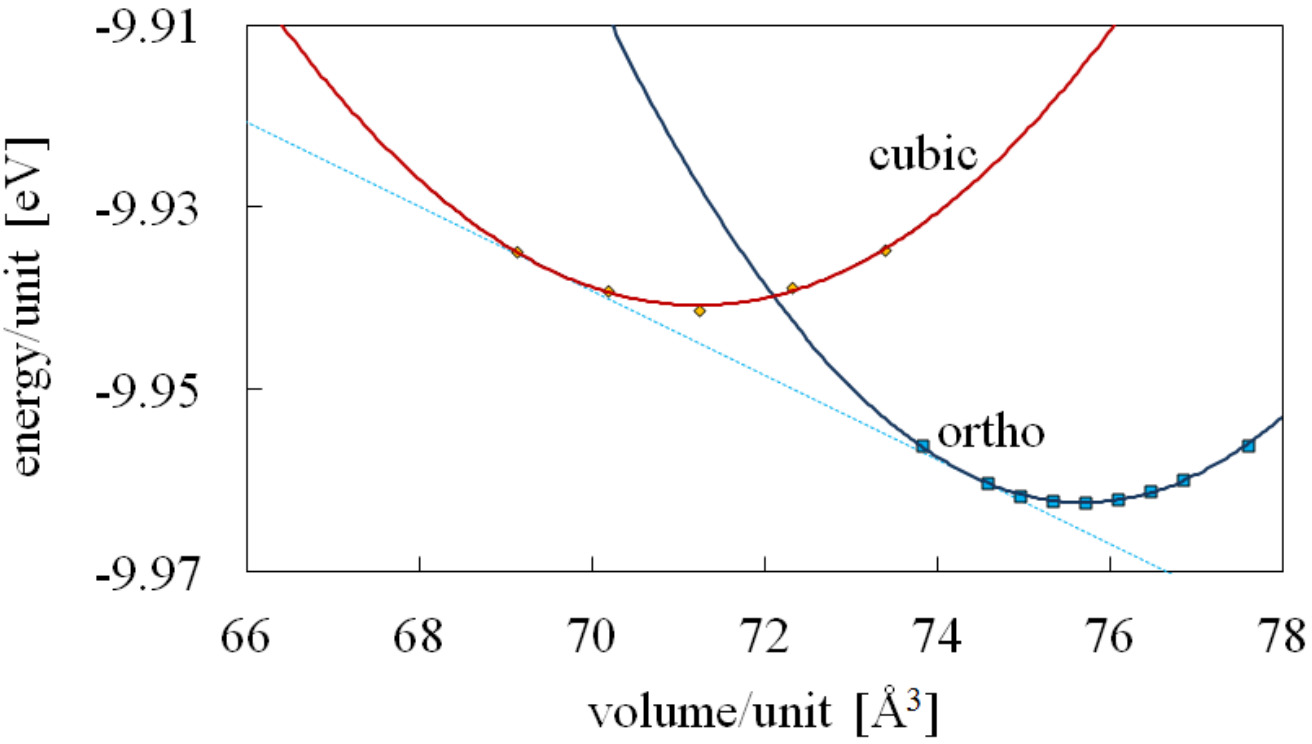

Figure 3 BP11518 11MAY2012

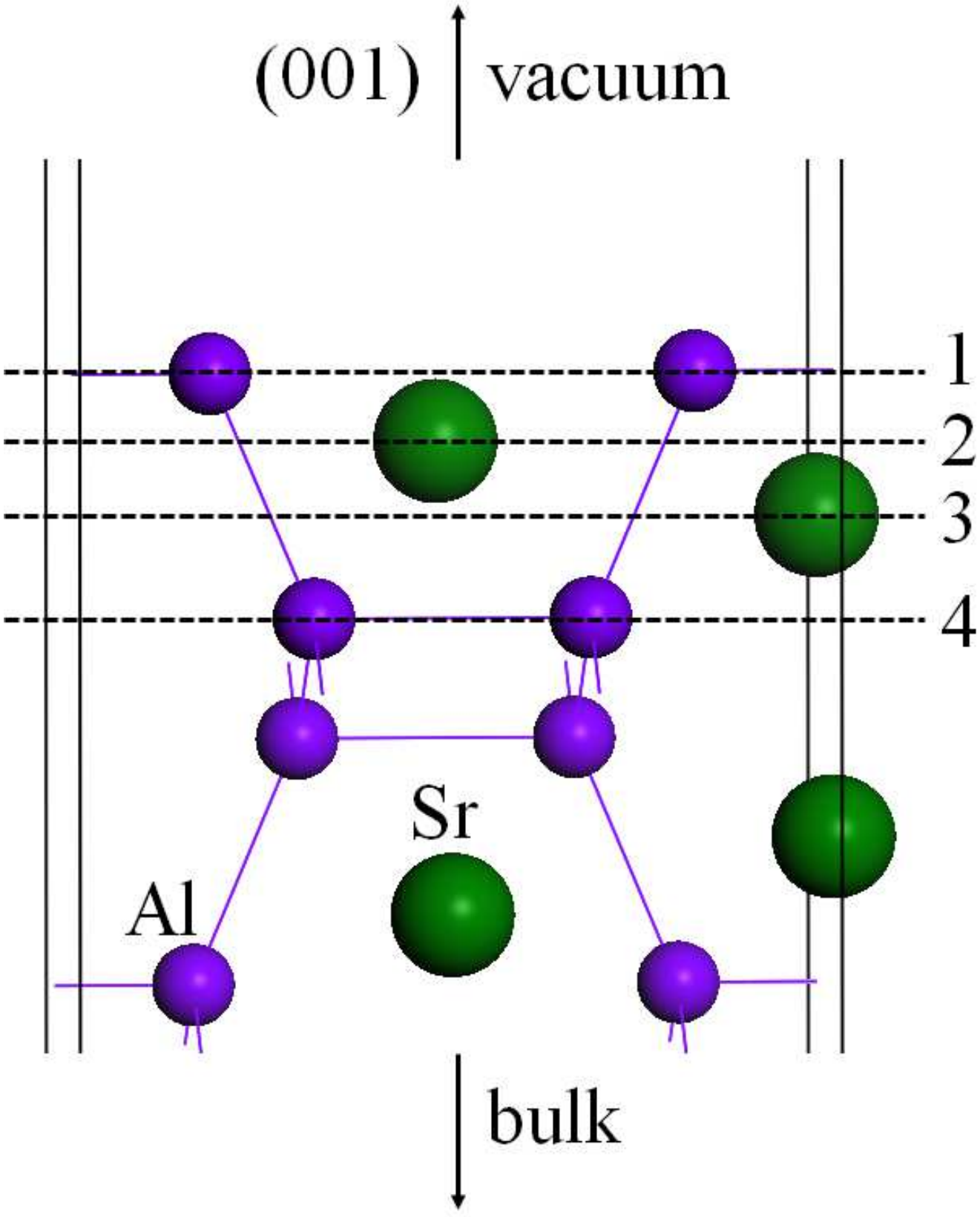

Figure 4a BP11518 11MAY2012

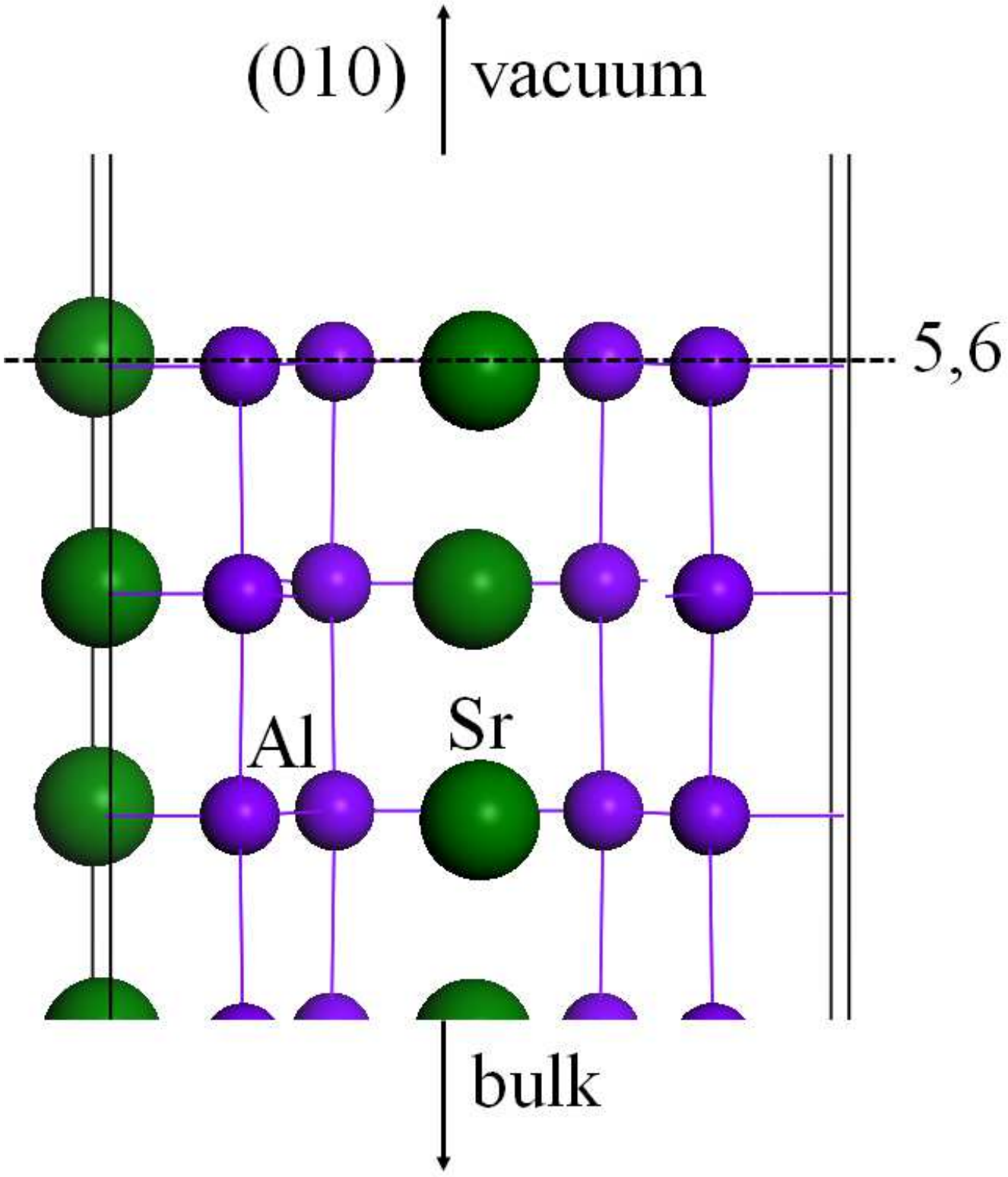

Figure 4b BP11518 11MAY2012

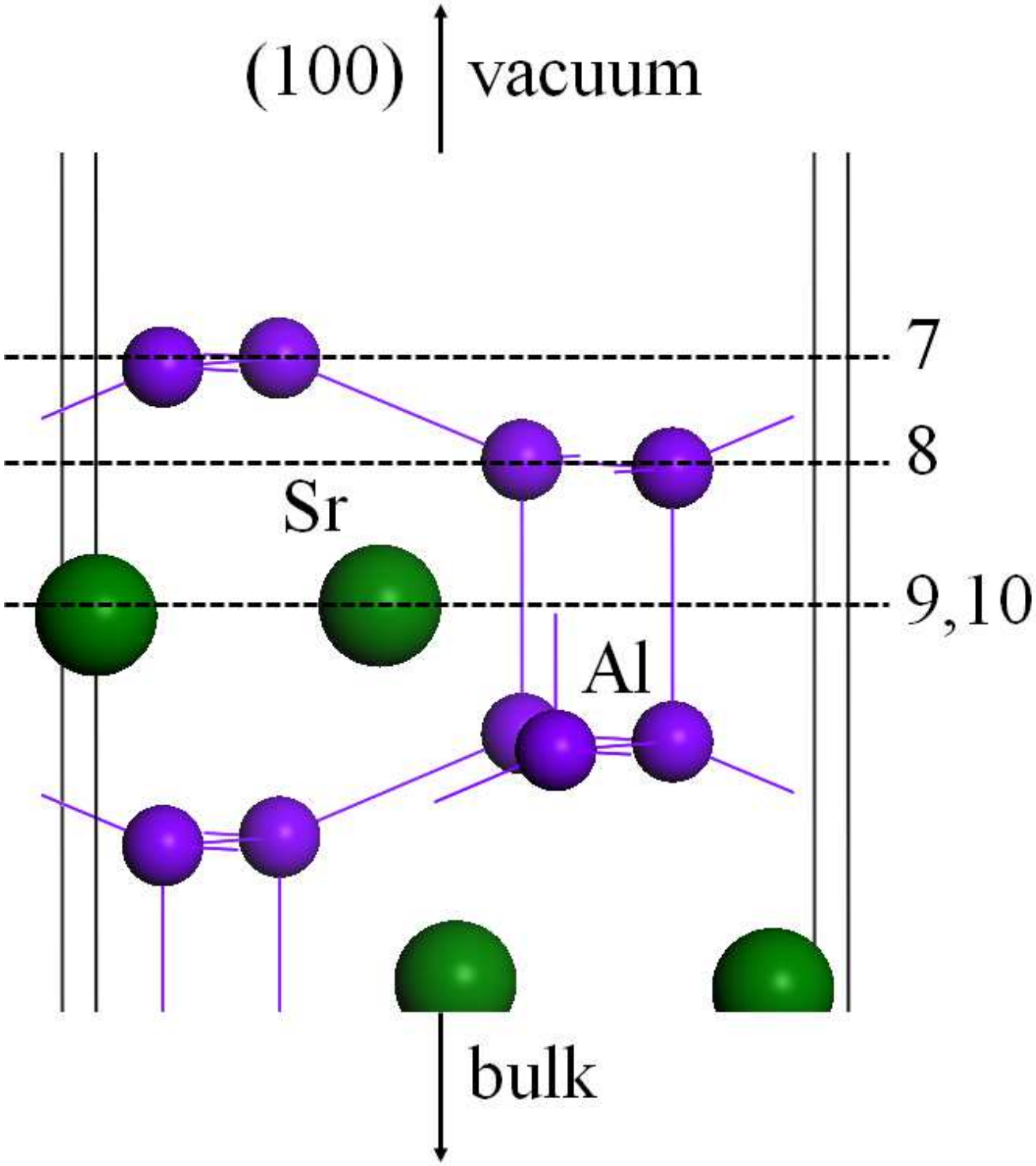

Figure 4c BP11518 11MAY2012

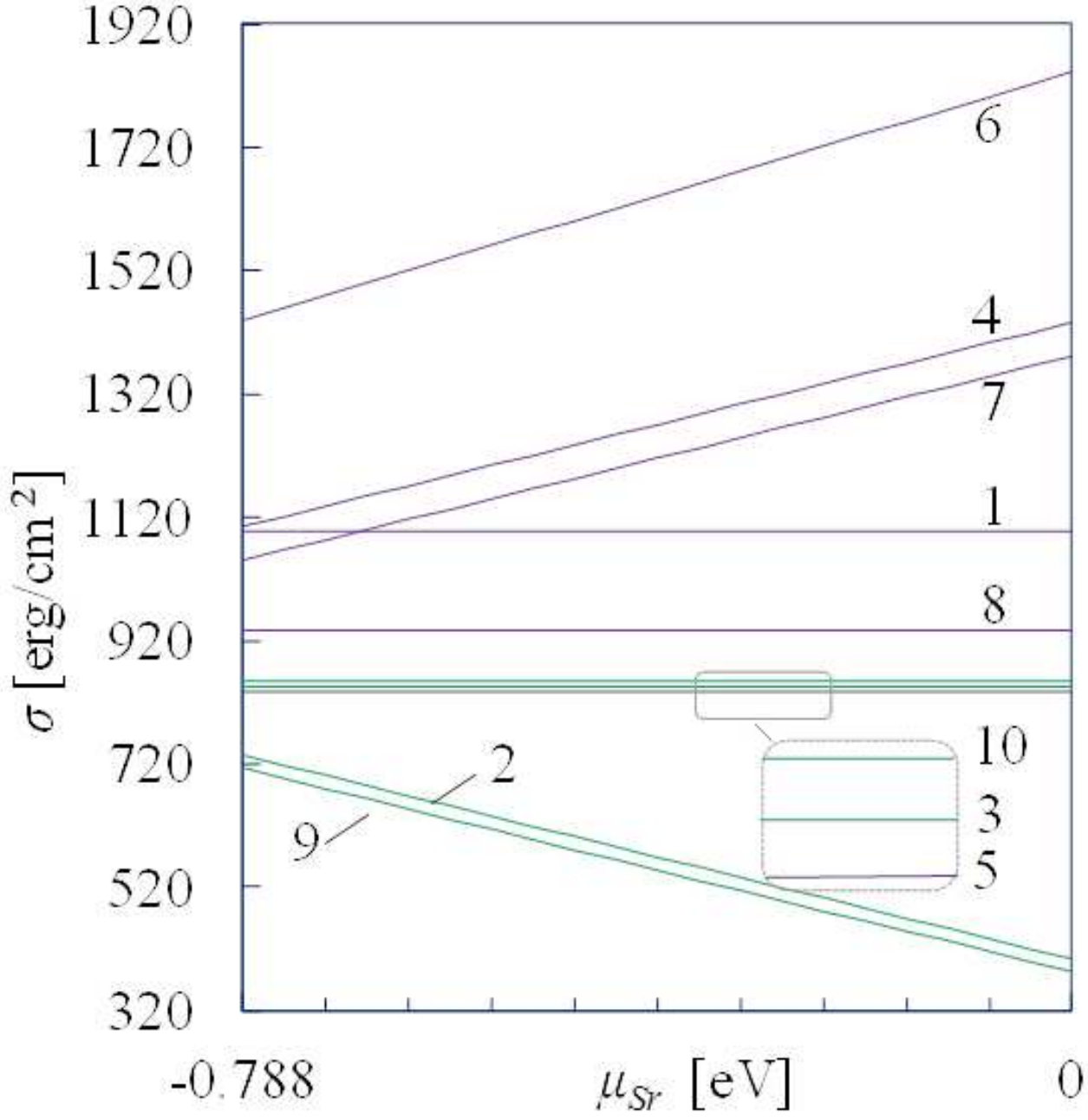

Figure 5a BP11518 11MAY2012

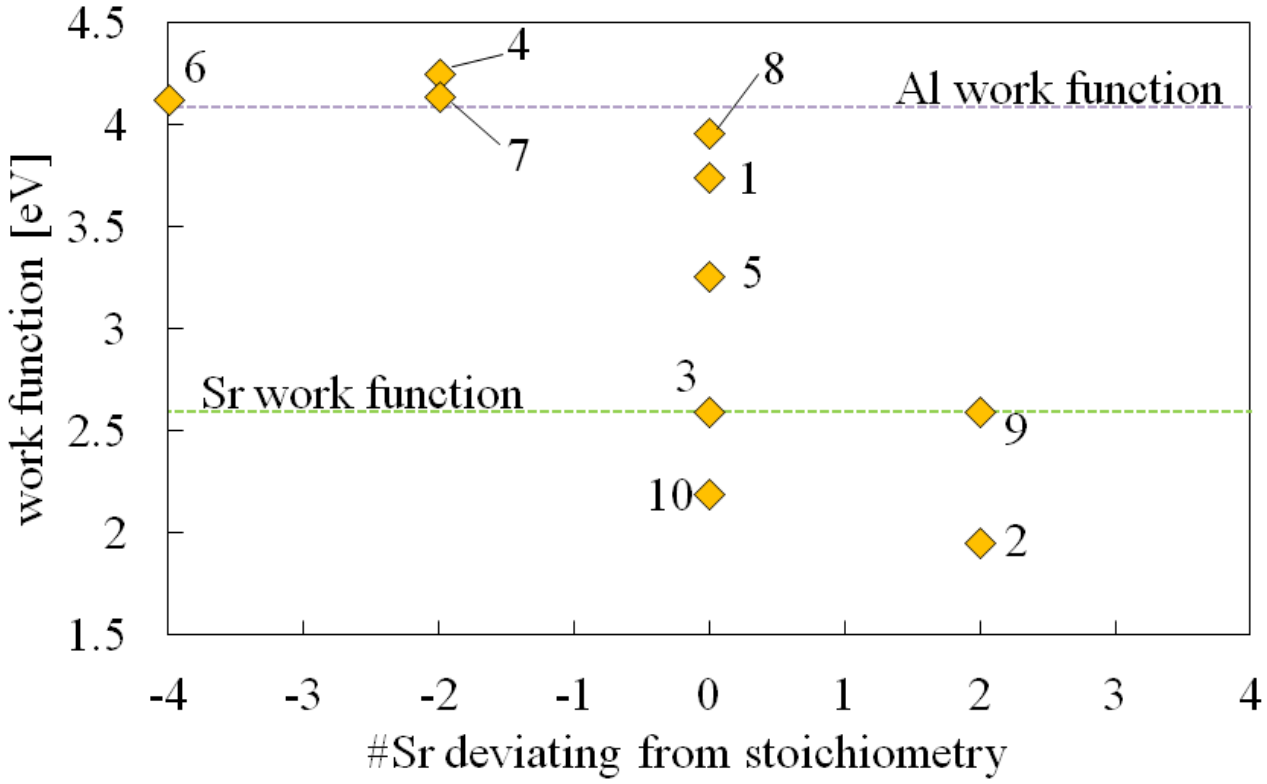

Figure 5b BP11518 11MAY2012